Journal of Energy Chemistry 52 (2021) 51–59

Contents lists available at ScienceDirect

Journal of Energy Chemistry

journal homepage: www.elsevier.com/locate/jechem

http://www.journals.elsevier.com/journal-of-energy-chemistry/

Surface defect-rich ceria quantum dots anchored on sulfur-doped carbon nitride nanotubes with enhanced charge separation for solar hydrogen production

Mengru Li, Changfeng Chen, Liping Xu, Yushuai Jia*, Yan Liu, Xin Liu*

Institute of Advanced Materials, College of Chemistry and Chemical Engineering, Jiangxi Normal University, Nanchang 330022, Jiangxi, China

ARTICLE INFO

Article history:
Received 24 February 2020
Revised 17 March 2020
Accepted 3 April 2020
Available online 25 April 2020

Keywords:
Photocatalytic hydrogen evolution
Ceria quantum dots
Sulfur-doped carbon nitride nanotubes
Surface defects
Charge separation

ABSTRACT

Designing defect-engineered semiconductor heterojunctions can effectively promote the charge carrier separation. Herein, novel ceria (CeO_2) quantum dots (QDs) decorated sulfur-doped carbon nitride nanotubes (SCN NTs) were synthesized via a thermal polycondensation coupled *in situ* deposition-precipitation method without use of template or surfactant. The structure and morphology studies indicate that ultrafine CeO_2 QDs are well distributed inside and outside of SCN NTs offering highly dispersed active sites and a large contact interface between two components. This leads to the promoted formation of rich Ce^{3+} ion and oxygen vacancies as confirmed by XPS. The photocatalytic performance can be facilely modulated by the content of CeO_2 QDs introduced in SCN matrix while bare CeO_2 does not show activity of hydrogen production. The optimal catalyst with 10% of CeO_2 loading yields a hydrogen evolution rate of 2923.8 μmol h^{-1} g^{-1} under visible light, remarkably higher than that of bare SCN and their physical mixtures. Further studies reveal that the abundant surface defects and the created 0D/1D junctions play a critical role in improving the separation and transfer of charge carriers, leading to superior solar hydrogen production and good stability.

1. Introduction

The increasing energy consumption and depletion of fossil resources have forced mankind to search for sustainable and clean energy [1]. Hydrogen is a promising clean energy for its environmental friendliness and high energy density. Photocatalytic hydrogen production from water utilizing renewable solar energy is recognized as an ideal route to address global energy and environment issues [2]. Although various materials such as metal oxides, sulfides, and nitrides have been reported for active hydrogen evolution, their efficiencies are still restricted by photocorrosion, poor visible light absorption, unsuitable band structure, and fast charge recombination [3,4].

As one of the most important rare earth material, ceria (CeO_2) has been extensively used as three-way catalysts, oxygen sensors, electrolytes, photoactive materals in solar cells, and photocatalysts for hydrogen generation and pollutant degradation [5,6]. This is mainly due to a variety of novel properties such as superior redox ability, high oxygen storage capacity, and physicochemical stability [7]. In particular, the valence change from Ce^{4+} to Ce^{3+} gives rise to the formation of oxygen vacancies on CeO_2 surface for keeping the charge balance, which are beneficial for visible light harvesting and charge carrier separation [8,9]. Hence the surface defects (Ce^{3+}/Ce^{4+} redox pairs and oxygen vacancies) in CeO_2 play an important role in improving the photocatalytic performance. Nevertheless, the inherently rapid recombination of electron-hole and severe aggregation of CeO_2 still restrict its photocatalytic efficiency in practical applications [10,11].

To accelerate the carrier separation and enhance the photocatalytic activity of CeO_2, one method is to fabricate stable nanostructured CeO_2 to regulate the surface defect structure [12,13]. For instance, quantum dots (QDs) possess particular properties of high surface energy, large surface area, abundant exposed atoms, and strong quantum confinement effect [14]. A high level of surface defects is inevitably produced when the size of CeO_2 is reduced to several nanometers, which can not only serve as the active sites for molecular adsorption and activation, but can also capture charges to suppress the recombination of electron-hole pairs [15,16]. However, at present most QDs should be synthesized and stabilized in the presence of organic surface ligands which may have detrimental effects on the catalytic activity [17,18].

* Corresponding authors.
E-mail addresses: ysjia@jxnu.edu.cn (Y. Jia), liuxin@jxnu.edu.cn (X. Liu).

https://doi.org/10.1016/j.jechem.2020.04.003

Construction of CeO_2 based heterojunctions coupled to other semiconductors is considered as another effective strategy to facilitate the charge transfer [10,19]. Polymeric carbon nitride (CN) has gained tremendous interest as an efficient metal-free photocatalytic material for hydrogen evolution [20]. In particular, it was reported that doping sulfur into CN framework could modify the electronic and optical properties as well as the carrier mobility of CN [21,22]. Previous studies showed that CN could form n-n junctions with CeO_2 by virtue of their matched band positions and the photocatalytic activity can be improved versus the single component [23–26]. Zou et al. reported a two-step self-assembly method to synthesize cubic CeO_2/CN composites with enhanced photocatalytic hydrogen evolution arising from the stronger interfacial effects [23]. Humayun et al. reported that the efficient elimination of 2,4-dichlorophenol was achieved over CeO_2/CN due to the greatly improved charge separation [24]. Liang and coworkers prepared CN@CeO_2 hollow heterostructure via a hard template method and found that the photocatalyst after H_2 reduction had rich oxygen vacancies and excellent photocatalytic activity for CO_2 reduction [25]. However, most of these works involved a complicated multistep process for the fabrication of CeO_2/CN junctions. Few literatures focused on the surface defects and the relationship of defect structure–photoactivity.

Here, aimed at modulating the defect structure and promoting the charge separation, we designed highly dispersed CeO_2 QDs/sulfur-doped CN nanotubes (SCN NTs) heterojunctions using an *in situ* deposition-precipitation strategy for superior visible-light photocatalytic hydrogen production. SCN NTs were prepared first through the thermal polymerization of supramolecular aggregates without use of template, and then CeO_2 QDs were *in situ* deposited on the inner and outer surfaces of SCN NTs. The introduction of SCN NTs not only provides more active sites for photocatalysis but also offers a tubular matrix for the dispersion and stabilization of ceria QDs. This leads to the activation of CeO_2 and the precise modulation of surface defects with abundant Ce^{3+} ions and oxygen vacancies, charge separation efficiency, and photocatalytic performances.

2. Experimental

2.1. Materials

Melamine, methanol, ammonium hydroxide, and cerium nitrate hexahydrate were purchased from Sinopharm Chemical Reagent Co., Ltd. Trithiocyanuric acid was supplied by Aladdin Industrial Corporation. All chemicals were of analytical grade and used as received.

2.2. Synthesis of SCN NTs

SCN NTs was prepared via the thermal polymerization of supramolecular aggregates [27]. Typically, equimolar amounts of trithiocyanuric acid and melamine were dispersed in a mixture solvent of deionized water and methanol, followed by ultrasonic treatment for 10 min and stirring at room temperature for 12 h. The yellow suspension was filtered, rinsed with deionized water, and dried at 70 °C. The resulting powder was finally annealed at 500 °C for 2 h in a tube furnace under Ar atmosphere.

2.3. Synthesis of CeO_2 nanoparticles (NPs)

CeO_2 NPs were synthesized by a deposition-precipitation method. 1 g of cerium nitrate hexahydrate was dissolved in 30 mL of deionized water forming a colorless and transparent solution. After dropwise addition of 5 mL of NH_3•H_2O under stirring, the resulting purple $Ce(OH)_3$ precipitate was filtered and dried at 60 °C, yielding the yellow product of CeO_2 [28], which was finally calcined at 250 °C for 4 h under Ar atmosphere.

2.4. Synthesis of CeO_2 QDs/SCN NTs

The fabrication process of CeO_2 QDs/SCN NTs is shown in Fig. 1. Different amounts of cerium nitrate hexahydrate were dissolved in deionized water. 500 mg SCN NTs were then dispersed into the $Ce(NO_3)_3$ solution under ultrasonication for 15 min followed by dropwise addition of NH_3•H_2O. The products were filtered, dried, and calcined at 250 °C for 4 h under Ar atmosphere. The obtained composites were denoted *x*% CeO_2/SCN where *x*% indicates the weight percent of CeO_2 in the hybrids.

2.5. Characterization

The crystal structure was analyzed by X-ray diffraction (XRD) patterns acquired using Cu *Kα* radiation (20 mA, 40 kV). The morphology and microstructure were investigated by a scanning electron microscopy (SEM, Hitachi) and a transmission electron microscopy (TEM, JEOL). The CeO_2 content in the composites was measured by a thermogravimetric analyzer (TGA, Diamond TG 6300) in air atmosphere. The optical properties were studied by UV-vis diffuse reflectance spectra (DRS) on a JASCO V-750 apparatus. The nitrogen sorption experiments were performed on a Micromeritics TriStar II 3020 analyzer to obtain the surface areas and pore size distributions of the catalysts. X-ray photoelectron spectroscopy (XPS) was carried out on an ESCALAB 250Xi apparatus. The peak positions were calibrated with the C 1s signal of contaminated carbon at 284.8 eV as the reference. The time-resolved photoluminescence (PL) decay spectra were excited at 325 nm and recorded at 460 nm with an Edinburgh FLS980 spectrometer.

Electrochemical measurements were performed on a CHI760E electrochemical workstation with a standard three-electrode cell in 0.5 M Na_2SO_4 electrolyte solution. The FTO glass, platinum wire, and Ag/AgCl electrode (in saturated KCl) were used as the working electrode, counter electrode, and reference electrode, respectively. The working electrode was prepared as follows: 10 mg photocatalyst was dispersed in 1 mL ethanol under sonication for 20 min with the addition of a drop of Nafion to make a slurry. The slurry was then coated onto a FTO glass (1 cm × 1 cm) and finally calcined at 150°C for 2 h.

2.6. Photocatalytic test

The photocatalytic hydrogen production experiments were performed in a quartz reactor connected to a closed circulating system. Typically, 50 mg photocatalyst was suspended in 100 mL aqueous solution containing 20 vol% triethanolamine (TEOA). The loading of 1 wt% Pt co-catalyst was conducted by *in situ* photodeposition of H_2PtCl_6. After evacuation for 30 min to remove the air, the system was irradiated with a 300-W Xe lamp equipped with a 400 nm cutoff filter. The reaction temperature was kept at 15 °C by using the cooling water. The generated gaseous products were quantified by a FuLi GC-9790 gas chromatograph with a thermal conductivity detector.

3. Results and discussion

3.1. Morphology and structure of CeO_2 QDs/SCN NTs

The crystal structures of SCN NTs, CeO_2 NPs, and CeO_2 QDs/SCN NTs were studied by XRD as displayed in Fig. 2(a). The diffraction peaks of CeO_2 NPs are located at 28.5°, 33.0°, 47.6°, 56.4°, 59.0°, 69.5°, 76.7°, 79.3°, and 88.6°, indexed to (111), (200), (220), (311), (222), (400), (331), (420), and (422) planes of cubic CeO_2 (JCPDS

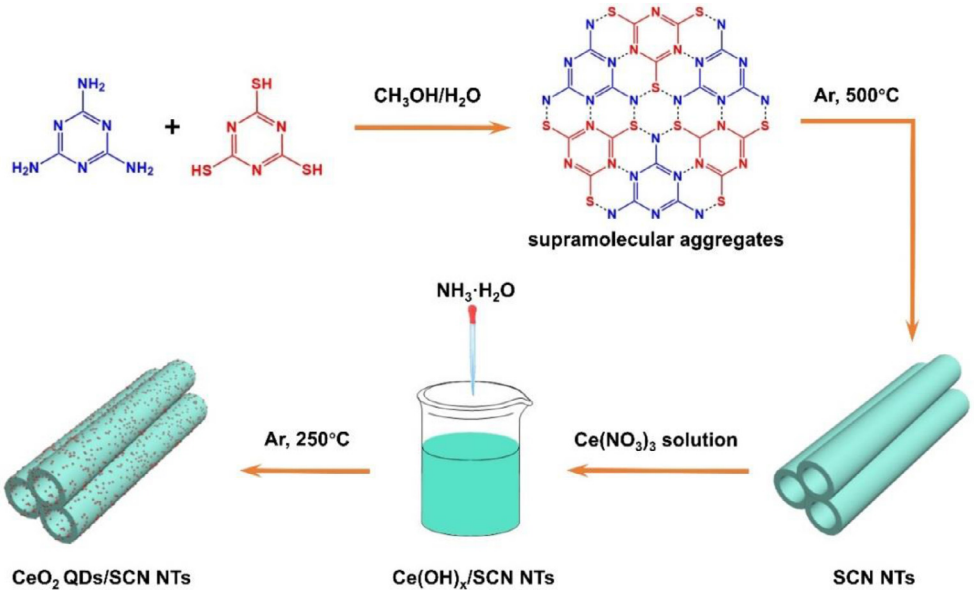

Fig. 1. Scheme of the synthesis of CeO_2 QDs/SCN NTs.

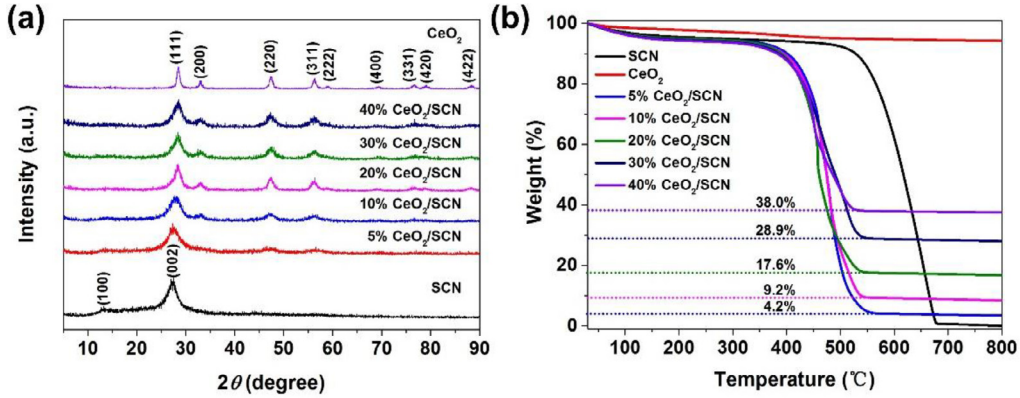

Fig. 2. (a) XRD patterns and (b) TGA curves of SCN, CeO_2, and CeO_2 QDs/SCN NTs.

no. 34-0394). Pristine SCN has two characteristic diffraction peaks at 13.3° and 27.5°, assigned to (100) plane of in-plane packing and (002) plane of interlayer stacking of aromatic system, respectively [20]. This indicates that the trithiocyanuric acid-melamine supramolecular aggregates have been polymerized to graphitic CN under the synthesis conditions. After decoration with CeO_2 QDs, the main peak of SCN at 27.5° overlaps with the strongest peak of CeO_2 at 28.5°. The CeO_2 characteristic peaks become stronger with increasing CeO_2 loading in the CeO_2/SCN composites. The peak positions of SCN have not changed but the peak intensity declines slightly. This reveals that the crystal structure of SCN is well maintained in the CeO_2 QDs/SCN NTs. Moreover, the CeO_2 diffraction peaks of CeO_2/SCN are obviously broader than that of CeO_2 NPs, indicative of a much smaller particle size based on the Debye-Scherrer equation [25].

The content of CeO_2 in CeO_2/SCN composites is measured by TGA in Fig. 2(b). No distinct weight loss is observed for pure CeO_2 NPs when it is heated up to 800 °C under air atmosphere. In contrast, SCN NTs begin to lose weight above 500 °C and burn out at about 680 °C. For CeO_2 QDs/SCN NTs, the decomposition temperature decreases below 350 °C because the introduction of CeO_2 accelerates the oxidation of SCN. Thus, the content of CeO_2 in CeO_2/SCN composites can be calculated from the residual mass after burning with values of 4.2%, 9.2%, 17.6%, 28.9%, and 38.0%, respectively, in accordance with the dosage of CeO_2 introduced.

The morphologies of the samples were investigated by SEM. As shown in Fig. 3(a and b), pure SCN with a hollow tube-like structure have been successfully fabricated. The SCN tubes have thin walls and possess a diameter from 200 to 500 nm and a length from 2 to 10 μm. Pristine CeO_2 are agglomerated NPs with a mean grain size of around 10–16 nm (Fig. 3c and d, Fig. S1). After loading of CeO_2, the tubular morphology was maintained, as illustrated in Fig. 3(e and f). No obvious CeO_2 particles are observed scanning across the whole specimen of 10% CeO_2/SCN. This implies that the SCN NTs may be decorated with very tiny CeO_2 particles forming uniformly dispersed and tightly contacted heterojunctions.

Fig. 4(a-c) shows the typical TEM images with different magnification of CeO_2 QDs/SCN NTs. Many black dots belonging to CeO_2 are homogeneously anchored on the inner and outer surfaces of 1D SCN NTs. The CeO_2 QDs in 10% CeO_2/SCN have an average particle size of about 2–3 nm, which is much smaller than pristine CeO_2 particles of 10–16 nm. This is due to the restrained aggregation and increased dispersion of CeO_2 crystals in SCN matrix and in line with the results obtained from XRD analysis. HRTEM image in Fig. 4(d) shows clear lattice fringes with a d-spacing of 0.31 nm, corresponding to the (111) plane of CeO_2 (JCPDS no. 34-0394).

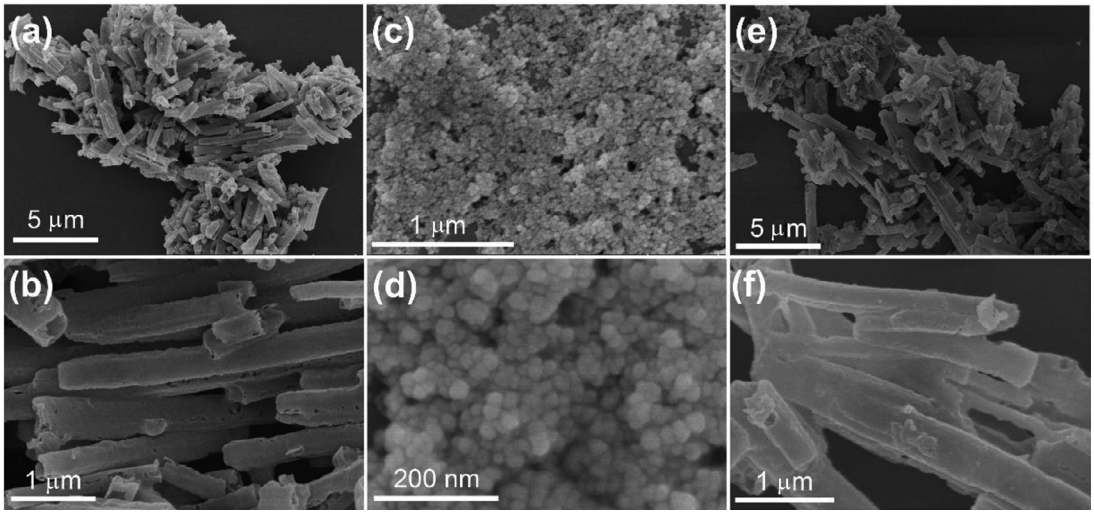

Fig. 3. SEM images of (a,b) SCN, (c,d) CeO_2, and (e,f) 10% CeO_2/SCN.

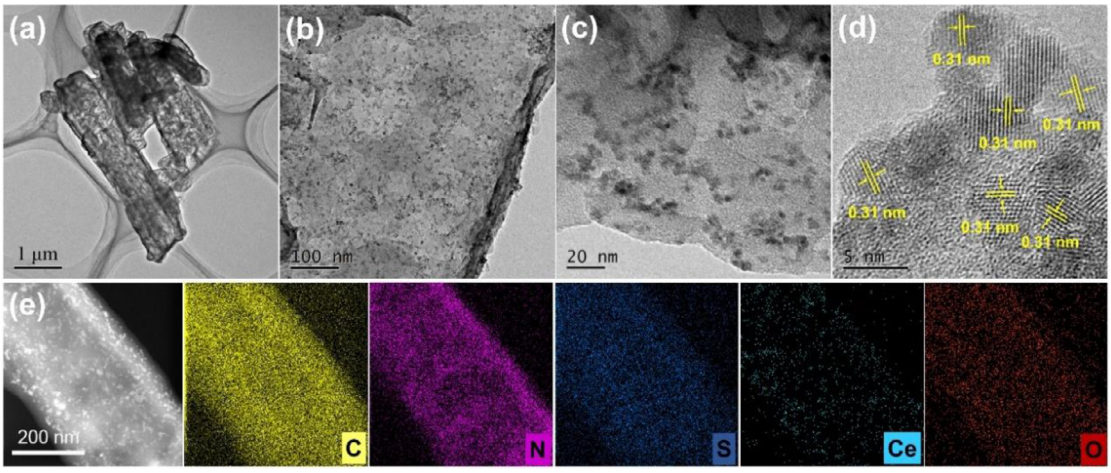

Fig. 4. (a-c) TEM images, (d) HRTEM image, and (e) EDS mapping images of 10% CeO_2/SCN.

Fig. 4(e) displays the dark field image of 10% CeO_2/SCN with the EDS mapping of C, N, S, Ce, and O. The sample clearly shows a hollow tubular morphology and all the elements are distributed evenly along the tubes. These results further confirm the formation of intimately contacted CeO_2/SCN heterojunctions with CeO_2 QDs uniformly deposited inside and outside of SCN NTs. This 0D/1D structure can offer more exposed active sites, large surface area, maximum interfacial contact, and high light scattering, which could further strengthen the synergistic effect between CeO_2 and SCN on improving the photocatalytic properties. In addition, this microstructure is also conducive to fast charge transport through the well-defined tubes, leading to accelerated carrier separation and enhanced photocatalytic performance.

The surface area and pore structure of SCN, CeO_2, and 10% CeO_2/SCN were studied by N_2 adsorption-desorption experiments. As shown in Fig. 5(a), all samples present characteristic type IV isotherms according to the IUPAC classification, suggesting the existence of mesoporous structures. The specific surface area of 10% CeO_2/SCN (59.1 m^2/g) is larger than that of pristine SCN (47.4 m^2/g) and pristine CeO_2 (55.5 m^2/g) due to the smaller particle size and higher dispersion of CeO_2. This indicates that 10% CeO_2/SCN can offer more active sites and reaction centers for catalytic reactions and would consequently show a better photocatalytic performance. The pore size distributions of pristine CeO_2 and SCN are centered at 3.7 and 29.1 nm, respectively, with the pores generated by the packing of CeO_2 particles and SCN tubes (Fig. 5b). Moreover, the BJH curve of 10% CeO_2/SCN is related to the combination of pristine SCN and CeO_2, further confirming that the pore structure of SCN in 10% CeO_2/SCN is unchanged after deposition of CeO_2 QDs, which is in agreement with the results of XRD, SEM, and TEM.

3.2. XPS analysis

The surface composition and chemical state of catalysts were further identified by XPS. The survey scan in Fig. 6(a) manifests the existence of C, N, O, and Ce in 10% CeO_2/SCN. Fig. 6(b) demonstrates that the C 1*s* spectra of SCN have three peaks at 284.8, 288.2, and 293.6 eV attributed to sp^2 C–C bonds of the surface adventitious carbon, sp^2-hybridized carbon of N=C–N, and π-excitation, respectively [8,29]. The N 1s spectra of SCN in Fig. 6(c) can be fitted into four peaks located at 398.6, 399.8, 401.1, and 404.5 eV, which can be assigned to sp^2-bonded nitrogen (C-N=C), sp^3-bonded nitrogen (N-$(C)_3$), amino functional groups, and charging effects, respectively [30,31]. Note that the C 1*s* and N 1*s* peaks of 10% CeO_2/SCN move to higher binding energies compared with pristine SCN, indicative of the strong interaction between intimately contacted CeO_2 QDs and SCN NTs in the heterojunctions. The signal of S 2*p* spectra is very weak due to a very low content (0.11%, Fig. 6d). The peaks at around 164 and 169 eV are related

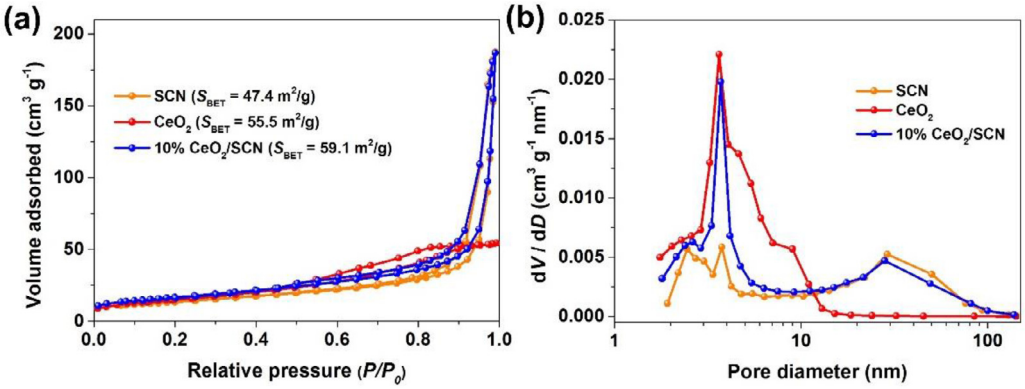

Fig. 5. (a) N_2 adsorption-desorption isotherms and (b) pore size distributions of SCN, CeO_2, and 10% CeO_2/SCN.

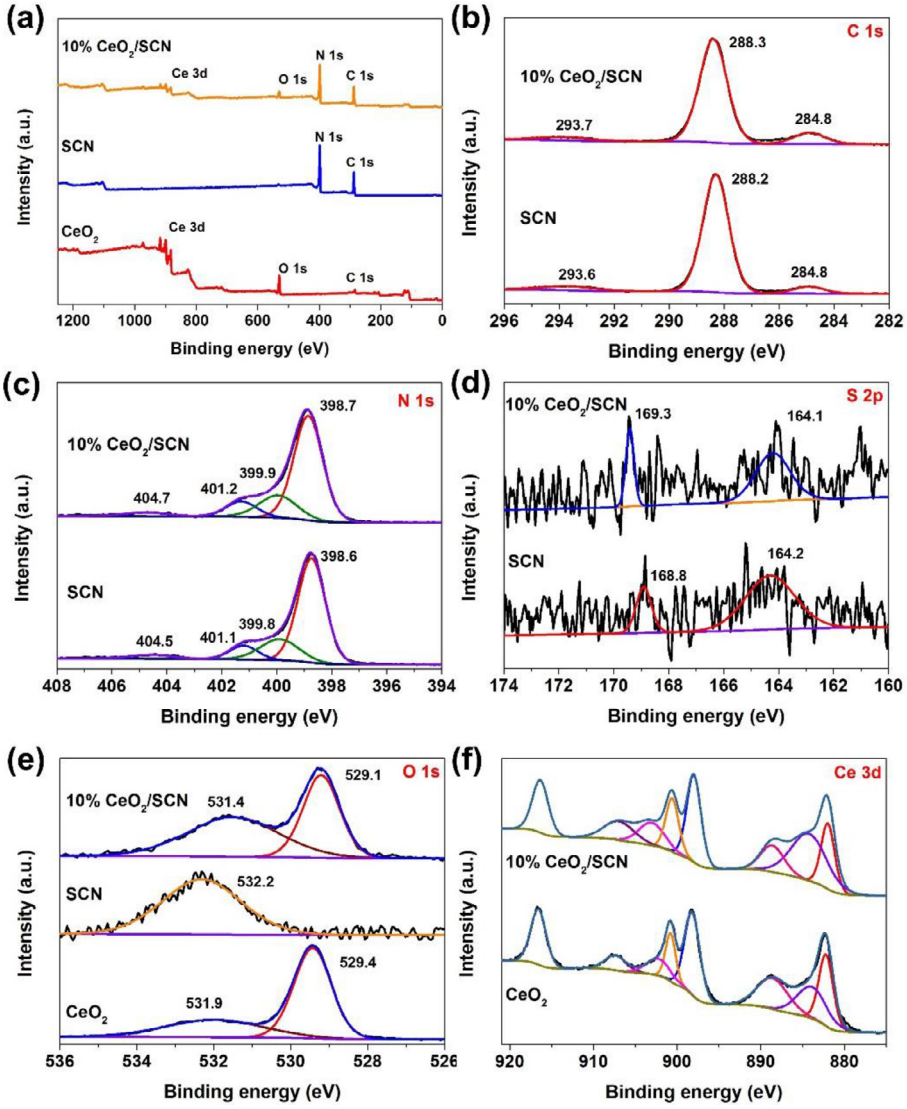

Fig. 6. XPS of SCN, CeO_2, and 10% CeO_2/SCN: (a) survey spectrum, (b) C 1*s*, (c) N 1*s*, (d) S 2*p*, (e) O 1*s*, and (f) Ce 3*d* spectra.

to the formation of S-N bonds in SCN framework and the sulfur oxide released during thermal polymerization [27]. The O 1*s* spectra in Fig. 6(e) show that pure SCN has a weak O 1*s* peak at 532.2 eV relevant to -OH group or chemisorbed H_2O [32]. The O 1*s* signals at around 529 and 531 eV for pristine CeO_2 and 10% CeO_2/SCN correspond to lattice oxygen and surface chemisorbed oxygen, respectively [33,34].

The high resolution spectra of Ce 3d can be deconvoluted into eight peaks (Fig. 6f). For pristine CeO_2, the peaks centered at 883.8 and 902.2 eV derive from $3d_{5/2}$ and $3d_{3/2}$ of Ce^{3+}, whereas those at

882.2, 888.6, and 898.2 eV are indexed to $3d_{5/2}$ of Ce^{4+} and those at 900.7, 907.3, and 916.5 eV are indexed to $3d_{3/2}$ of Ce^{4+} [35,36]. For 10% CeO_2/SCN, the binding energies of Ce^{3+} (884.1 and 902.9 eV) are much higher than that of pristine CeO_2 while the peaks of Ce^{4+} shift to lower binding energies (881.9, 888.5, 897.8, 900.5, 906.9, and 916.3 eV). The peak shifts are probably due to the chemical state change of Ce ions in 10% CeO_2/SCN [16]. The coexistence of Ce^{3+} and Ce^{4+} indicates the generation of Ce^{3+}/Ce^{4+} redox electron pairs on the catalyst surface, which is favorable for the storage and release of reactive oxygen species [8,37]. The concentration of Ce^{3+} is calculated using the relative peak area of Ce^{3+} and Ce^{4+} [38], with values of 21.5% and 31.6% for pristine CeO_2 and 10% CeO_2/SCN, respectively. More Ce^{3+} ions are produced in 10% CeO_2/SCN than in pristine CeO_2 particles because of the smaller size and more exposed surface of CeO_2 QDs. Therefore, the density of surface defects in CeO_2 can be regulated via the CeO_2-SCN heterojunction construction and hence results in the regulation of photocatalytic activity.

In general, Ce^{3+} ions and surface oxygen vacancies appear synchronously in ceria for keeping the charge balance [39,40]:

$$2Ce^{4+} + O_L = 2Ce^{3+} + O_V + 1/2O_2(g). \quad (1)$$

Where O_L and O_V represent the oxygen atom of lattice oxygen and the oxygen vacancy with charge of plus two, respectively. Therefore, the obviously higher content of Ce^{3+} in 10% CeO_2/SCN indicates that more surface oxygen vacancies are generated which favors the adsorption and activation of water molecules in photocatalytic water splitting [11,16]. Moreover, oxygen vacancies can serve as the capture centers for photogenerated electrons that consequently suppress the recombination of electron-hole pairs [41,42]. This would lead to enhanced photocatalytic activity of 10% CeO_2/SCN because of a higher content of Ce^{3+} and oxygen vacancies compared with pristine CeO_2 NPs.

3.3. Photocatalytic hydrogen evolution

The catalytic performances of CeO_2/SCN composites were evaluated by the photocatalytic hydrogen evolution reaction (HER) under visible-light irradiation. As depicted in Fig. 7(a and b), pristine CeO_2 is inactive in hydrogen production from water splitting due to the severe recombination of charge carriers. Pristine SCN shows a steady H_2 evolution with a total amount of 293.24 μmol and a HER rate of 1466.2 μmol h^{-1} g^{-1} after 4 h of irradiation. The dispersion of CeO_2 QDs on SCN NTs leads to the precise modulation of photocatalytic performances. The HER rate first rises and then declines as the CeO_2 loading increases from 5% to 40%. More specifically, the highest activity is achieved over 10% CeO_2/SCN with a HER rate up to 2923.8 μmol h^{-1} g^{-1}, which is 2 times higher than pristine SCN NTs. This HER value is much larger than that of most CN or CeO_2 based photocatalysts reported previously, such as TiO_2/CN [43], Cu_2O/CN [44], CeO_2/carbon [45], CdS/CeO_2 [46], CeO_2/CN [47]. On account of the inactivity of bare CeO_2, the creation of homogeneous CeO_2/SCN heterojunctions gives rise to the activation of CeO_2 for photocatalytic hydrogen evolution. Moreover, only a small amount of CeO_2 with 10% loading is used for the regulation of optimal performance because CeO_2 QDs is evenly dispersed and have intimate interaction with SCN NTs. In contrast, excess CeO_2 QDs will cover the active sites on SCN surface and act as the recombination center for photogenerated electron-hole pairs [48]. This has resulted in the activity decline as CeO_2 content exceeding 10%.

For comparison, the performances of the physical mixture of SCN and CeO_2 are also tested. Fig. 7(c) shows that the H_2 evolution over CeO_2-SCN mixture is also enhanced but less efficient compared with CeO_2/SCN hybrids, and the optimal CeO_2 content turns out to be 30%. This is mainly ascribed to the poor contact and bad dispersion of CeO_2 NPs on SCN NTs by the simple physical mixing. These results indicate that the dispersion of CeO_2 and interfacial contact between the two components play crucial roles in the activity enhancement of CeO_2/SCN composites.

Table 1. Fitting results of PL decay curves.

Sample	A_1	τ_1 (ns)	A_2	τ_2 (ns)	χ^2
SCN	0.038	1.68	0.004	9.75	1.221
10% CeO_2/SCN	0.062	1.88	0.007	10.51	1.138

To explore the stability of the photocatalyst, a long-time experiment of 10% CeO_2/SCN is performed under the same conditions. As shown in Fig. 7(d), the amount of H_2 is increased linearly within 14 h of visible-light irradiation. The sample was then collected after stability experiment and used for XRD, TEM, and XPS characterization, which demonstrate that the crystal structure, morphology, and chemical states of 10% CeO_2/SCN are almost unchanged after photocatalytic reaction (Figs. 8 and S2). In addition, the concentration of Ce^{3+} in the used sample is calculated to be 30.9% (Fig. S2), nearly identical to that of the fresh one (31.6%). These results clearly show that 10% CeO_2/SCN is a stable photocatalyst for solar hydrogen production.

3.4. Photocatalytic mechanism

It is reported that the surface defects and the junction creation are conductive to promoting the interfacial charge transfer in photocataysis [11,49]. The charge separation efficiency was evaluated by the electrochemical impedance spectra (EIS) and transient photocurrent responses. Fig. 9(a) shows the Nyquist EIS plots of the as-prepared samples under visible light. Generally, a smaller arc radius implies a lower interfacial charge-transfer resistance and hence a higher charge transfer efficiency [50]. Compared with pristine SCN, 10% CeO_2/SCN shows a much smaller arc radius, indicative of the promoted carrier separation. In addition, 10% CeO_2/SCN displays obviously bigger photocurrent than SCN and CeO_2 (Fig. 9b), validating that the generation of abundant surface defects and the intimate heterojunctions between CeO_2 QDs and SCN NTs can greatly accelerate the separation of photogenerated charge carriers.

Furthermore, time-resolved PL decay curves were measured to probe the charge transfer dynamics of the samples [51]. As exhibited in Fig. 9(c), the time-resolved PL spectra of SCN and 10% CeO_2/SCN show obvious decay while the PL signal of CeO_2 is too weak to measure the attenuation. The plots were well fitted by the following equation with two decay components [52,53]:

$$I(t) = A_1 \exp\left(\frac{-t}{\tau_1}\right) + A_2 \exp\left(\frac{-t}{\tau_2}\right) \quad (2)$$

Where $I(t)$, τ, and A represent the PL intensity, the lifetime, and the pre-exponential factor, respectively. The fitting results are listed in Table 1. Note that 10% CeO_2/SCN has much larger values of τ_1 and τ_2 (1.88, 10.51 ns) than pristine SCN (1.68, 9.75 ns) revealing a slower PL attenuation with longer carrier lifetime. This further indicates faster charge separation and thus higher photocatalytic performance for 10% CeO_2/SCN.

The optical absorption properties were characterized by UV-vis DRS (Fig. 10a). The absorption edges of SCN and CeO_2 are located at 469 and 475 nm. The CeO_2/SCN composite samples have absorption curves similar to pristine SCN. A tailing absorption ranging from 450 to 600 nm is observed for the composites and SCN due to the modification of light harvesting by S doping [54]. The band gap energies of SCN and CeO_2 are calculated according to the Tauc relationship using the absorption data by the following formula [55]:

$$\alpha h\nu = A\ (h\nu - E_g)^{n/2} \quad (3)$$

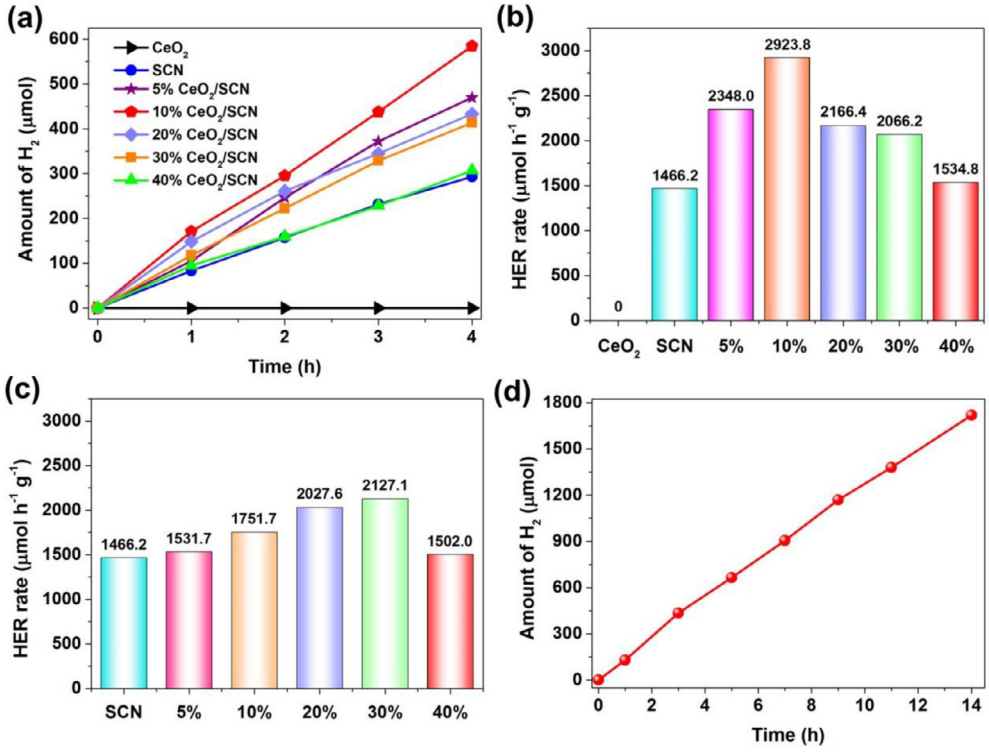

Fig. 7. (a) Time course of H_2 production and (b) HER rates of SCN, CeO_2, and CeO_2/SCN composites. (c) HER rates of the mechanical mixture of SCN and CeO_2 with different CeO_2 contents. (d) Long-time H_2 evolution of 10% CeO_2/SCN.

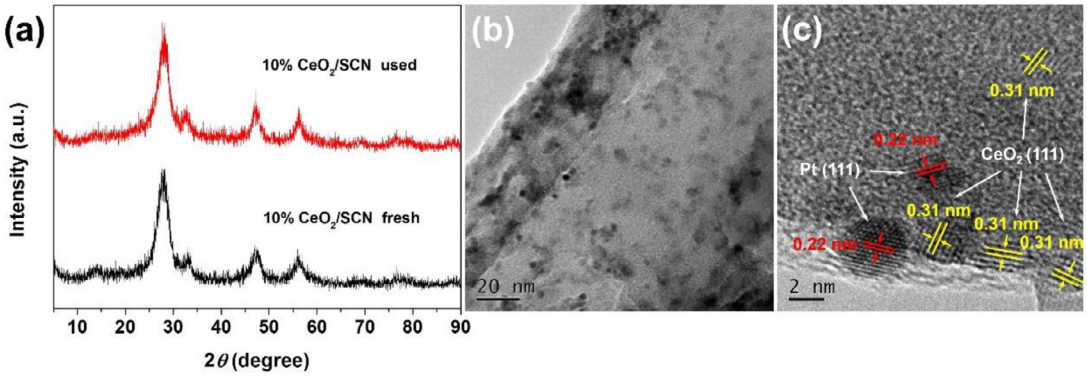

Fig. 8. (a) XRD patterns, (b) TEM image, and (c) HRTEM image of 10% CeO_2/SCN collected after 14 h reaction.

Where α, ν, h, and E_g refer to the absorption coefficient, light frequency, Planck constant, and band gap energy, respectively. A is a proportionality constant. n lies on the optical transition type of semiconductors with values of 4 and 1 for SCN and CeO_2, respectively [56,57]. The Tauc curves are then plotted with band gap energies determined to be 2.42 and 2.76 eV for SCN and CeO_2, respectively (Fig. 10b).

The valence band (VB) XPS spectra were measured to determine the band structure of SCN and CeO_2 (Fig. 11a), which demonstrate values of 2.10 and 2.04 eV assigned to the energy difference ($\Delta E_{F\text{-}VB}$) between VB and the Fermi level [58]. The valence band maxima (VBM) of SCN and CeO_2 are estimated to be 1.76 and 2.23 V using the formula $E_{RHE}/V = \Phi + \Delta E_{F\text{-}VB} - 4.44$ (E_{RHE}: potential of standard hydrogen electrode, Φ: the electron work function (4.10 and 4.63 eV for SCN and CeO_2)) [59,60]. Combined with their band gap energies, the conduction band minima (CBM) of SCN and CeO_2 are calculated to be -0.66 and -0.53 V, respectively. The CBM and VBM potentials of SCN are shown to be more negative than that of CeO_2. Due to their well-matched band positions, the decoration of CeO_2 QDs on SCN tubes results in the formation of Type II heterojunctions at the composite interfaces [61].

The possible mechanism of the enhanced photocatalytic hydrogen evolution of 10% CeO_2/SCN is depicted in Fig. 11(b). When the composite is illuminated by visible light, both SCN and CeO_2 can be excited by photons with energy higher than their band gaps and produce photogenerated electrons and holes. Driven by the built-in electric field at the interfaces, the holes in the VB of CeO_2 would easily transfer to SCN with a more negative VBM potential; the electrons in the CB of SCN quickly migrate into CeO_2, leading to efficient spatial separation of charge carriers on the heterojunction interfaces. Then, the separated holes on SCN can oxidize TEOA into $TEOA^+$; the electrons on CeO_2 are captured by Pt particles and reduce H^+ to large amount of hydrogen. Meanwhile, the accumulated electrons on CeO_2 will result in partial reduction of Ce^{4+} to Ce^{3+}, while the holes on SCN can further oxidize Ce^{3+} to Ce^{4+}, leading to the cycle of Ce^{3+}/Ce^{4+} redox pairs with constant Ce^{3+} content as confirmed by XPS. Therefore, the presence of abundant Ce^{3+} and

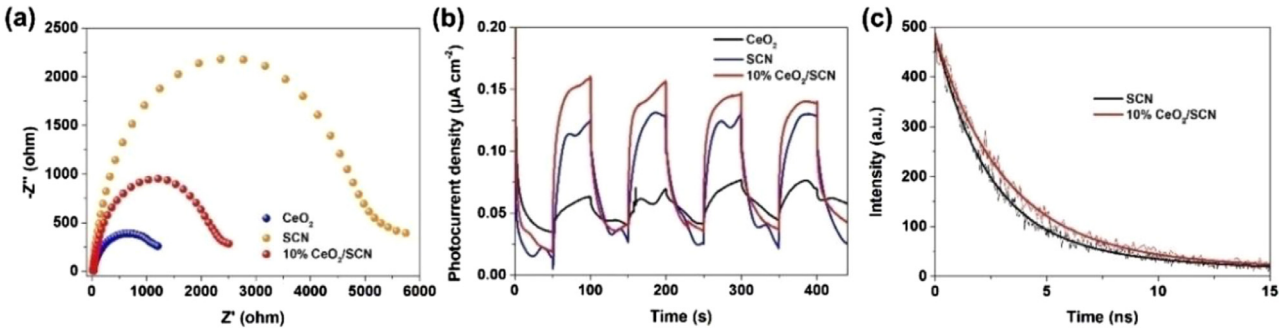

Fig. 9. (a) EIS plots, (b) transient photocurrent curves, and (c) time-resolved PL decay curves of SCN, CeO_2, and 10% CeO_2/SCN.

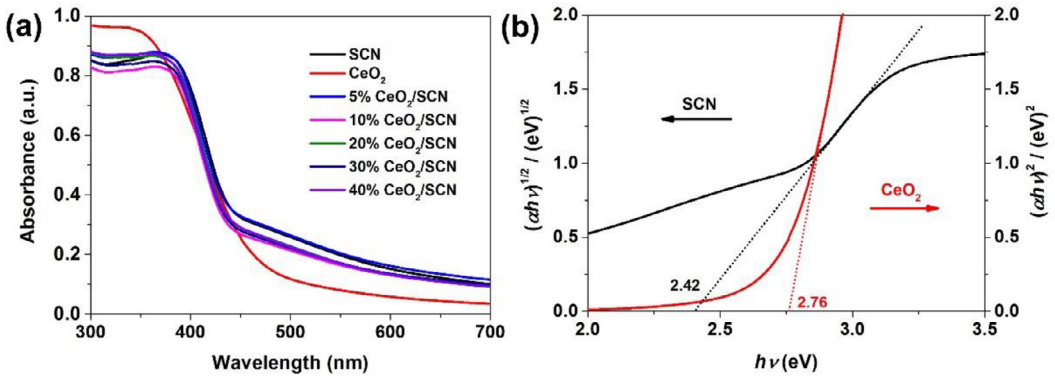

Fig. 10. (a) UV-vis DRS of SCN, CeO_2, and CeO_2 QDs/SCN NTs. (b) Tauc plots of SCN and CeO_2.

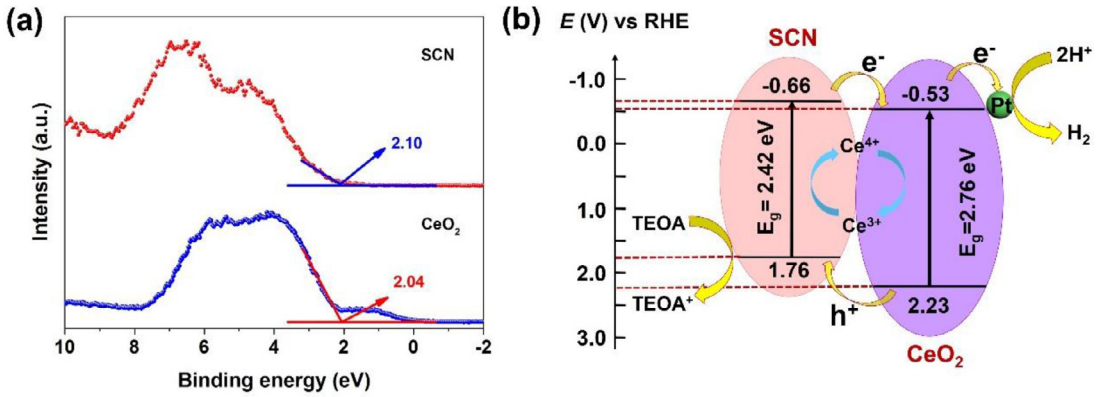

Fig. 11. (a) VB spectra of SCN and CeO_2. (b) Schematic illustration of the proposed photocatalytic mechanism of CeO_2/SCN heterojunctions under visible light illumination.

oxygen vacancies could greatly suppress the electron-hole recombination, giving rise to considerably enhanced photocatalytic activity compared with pristine SCN and CeO_2.

4. Conclusions

In summary, we developed a facile thermal polycondensation coupled *in situ* deposition-precipitation strategy for the synthesis of Type II CeO_2/SCN heterojunctions with improved photocatalytic performance. The homogeneous dispersion of CeO_2 QDs on the inner and outer surfaces of SCN tubes promotes the formation of surface defect structure with a high content of Ce^{3+} ions and oxygen vacancies, which leads to the activation of CeO_2 and precise modulation of the charge separation efficiency and photocatalytic performances. The HER rate first rises and then declines as the CeO_2 loading increases. The highest activity is observed over 10% CeO_2/SCN with a HER rate of 2923.8 μmol h^{-1} g^{-1}, significantly higher than that of pristine SCN and their physical mixtures. In addition, the sample shows a steady H_2 evolution under long-time visible-light irradiation up to 14 h without obvious activity decrease and structure change. Such an activity improvement relates to the unique structure with many favorable properties. The 0D/1D structure can offer more exposed active sites, large surface area, maximum interfacial contact, and high light scattering, producing the synergistic effect between CeO_2 and SCN on improving the photocatalytic properties. In addition, the Type II heterostructure with abundant surface defects are conducive to interfacial charge separation and transport along the well-defined tubes, leading to accelerated carrier transfer efficiency and enhanced photocatalytic performance. This work offers a novel strategy to design hybrid materials with boosted performance by surface defect engineering and heterojunction creation which can be potentially applied in heterogeneous catalysis and solar energy conversion.

Acknowledgments

This work was financially supported by the National Natural Science Foundation of China (21872065, 21763013, and 21503100), the Natural Science Foundation of Jiangxi Province (20192ACBL21027 and 20192BAB203007), and the Project of Education Department of Jiangxi Province (GJJ170227).

Supplementary materials

Supplementary material associated with this article can be found, in the online version, at doi:10.1016/j.jechem.2020.04.003.

References

[1] T. Hisatomi, J. Kubota, K. Domen, Chem. Soc. Rev. 43 (2014) 7520–7535.
[2] Z. Wang, C. Li, K. Domen, Chem. Soc. Rev. 48 (2019) 2109–2125.
[3] X. Li, J.G. Yu, M. Jaroniec, Chem. Soc. Rev. 45 (2016) 2603–2636.
[4] K. Afroz, M. Moniruddin, N. Bakranov, S. Kudaibergenov, N. Nuraje, J. Mater. Chem. A 6 (2018) 21696–21718.
[5] P.F. Ji, J.L. Zhang, F. Chen, M. Anpo, J. Phys. Chem. C 112 (2008) 17809–17813.
[6] Z.M. Yang, G.F. Huang, W.Q. Huang, J.M. Wei, X.G. Yan, Y.Y. Liu, C. Jiao, Z. Wan, A. Pan, J. Mater. Chem. A 2 (2014) 1750–1756.
[7] L.H. Jiang, M.G. Yao, B. Liu, Q.J. Li, R. Liu, H. Lv, S.C. Lu, C. Gong, B. Zou, T. Cui, B.B. Liu, J. Phys. Chem. C 116 (2012) 11741–11745.
[8] M.L. Li, L.X. Zhang, M.Y. Wu, Y.Y. Du, X.Q. Fan, M. Wang, L.L. Zhang, Q.L. Kong, J.L. Shi, Nano Energy 19 (2016) 145–155.
[9] P. Zhang, Y. Liu, B.Z. Tian, Y.S. Luo, J.L. Zhang, Catal. Today 281 (2017) 181–188.
[10] K. Saravanakumar, R. Karthik, S.M. Chen, J.V. Kumar, K. Prakash, V. Muthuraj, J. Colloid Interface Sci. 504 (2017) 514–526.
[11] W.X. Zou, B. Deng, X.X. Hu, Y.P. Zhou, Y. Pu, S.H. Yu, K.L. Ma, J.F. Sun, H.Q. Wan, L. Dong, Appl. Catal. B 238 (2018) 111–118.
[12] M.M. Khan, S.A. Ansari, D. Pradhan, D.H. Han, J. Lee, M.H. Cho, Ind. Eng. Chem. Res. 53 (2014) 9754–9763.
[13] D. Luo, B.B. Chen, X.Y. Li, Z.J. Liu, X.W. Liu, X.H. Liu, C. Shi, X.S. Zhao, J. Mater. Chem. A 6 (2018) 7897–7902.
[14] K.A.S. Fernando, S. Sahu, Y.M. Liu, W.K. Lewis, E.A. Guliants, A. Jafariyan, P. Wang, C.E. Bunker, Y.P. Sun, ACS Appl. Mater. Interfaces 7 (2015) 8363–8376.
[15] W. Zhou, H.G. Fu, Inorg. Chem. Front. 5 (2018) 1240–1254.
[16] N. Zhang, C. Gao, Y.J. Xiong, J. Energy Chem. 37 (2019) 43–57.
[17] Y.D. Yin, A.P. Alivisatos, Nature 437 (2005) 664–670.
[18] S.Y. Lim, W. Shen, Z.Q. Gao, Chem. Soc. Rev. 44 (2015) 362–381.
[19] X.Z. Li, W. Zhu, X.W. Lu, S.X. Zuo, C. Yao, C.Y. Ni, Chem. Eng. J. 326 (2017) 87–98.
[20] X.C. Wang, K. Maeda, A. Thomas, K. Takanabe, G. Xin, J.M. Carlsson, K. Domen, M. Antonietti, Nat. Mater. 8 (2009) 76–80.
[21] X.C. Wang, S. Blechert, M. Antonietti, ACS Catal. 2 (2012) 1596–1606.
[22] L.B. Jiang, X.Z. Yuan, Y. Pan, J. Liang, G.M. Zeng, Z.B. Wu, H. Wang, Appl. Catal. B 217 (2017) 388–406.
[23] W.X. Zou, Y. Shao, Y. Pu, Y.D. Luo, J.F. Sun, K.L. Ma, C.J. Tang, F. Gao, L. Dong, Appl. Catal. B 218 (2017) 51–59.
[24] M. Humayun, Z.W. Hu, A. Khan, W. Cheng, Y. Yuan, Z.P. Zheng, Q.Y. Fu, W. Luo, J. Hazard. Mater. 364 (2019) 635–644.
[25] M.F. Liang, T. Borjigin, Y.H. Zhang, B.H. Liu, H. Liu, H. Guo, Appl. Catal. B 243 (2019) 566–575.
[26] R. Ma, S. Zhang, L. Li, P.C. Gu, T. Wen, A. Khan, S.J. Li, B.F. Li, S.H. Wang, X.K. Wang, ACS Sustain. Chem. Eng. 7 (2019) 9699–9708.
[27] Y. Zheng, Z.H. Yu, F. Lin, F.S. Guo, K.A. Alamry, L.A. Taib, A.M. Asiri, X.C. Wang, Molecules 22 (2017) 572–588.
[28] Z. Liu, X.J. Li, M. Mayyas, P. Koshy, J.N. Hart, C.C. Sorrell, Cryst.Eng.Comm. 19 (2017) 4766–4776.
[29] A.L. Jin, Y.S Jia, C.F. Chen, X. Liu, J.Z. Jiang, X.S. Chen, F. Zhang, J. Phys. Chem. C 121 (2017) 21497–21509.
[30] M. Jourshabani, Z. Shariatinia, A. Badiei, J. Colloid Interface Sci. 507 (2017) 59–73.
[31] A.L. Jin, X. Liu, M.R. Li, Y.S. Jia, C.F. Chen, X.S. Chen, ACS Sustain. Chem. Eng. 7 (2019) 5122–5133.
[32] N.A. Mohamed, J. Safaei, A.F. Ismail, M.F.M. Noh, N.A. Arzaee, N.N. Mansor, M.A. Ibrahim, N.A. Ludin, J.S. Sagu, M.A.M. Teridi, J. Alloy. Comp. 818 (2020) 152916.
[33] R.H. Gao, D.S. Zhang, P. Maitarad, L.Y. Shi, T. Rungrotmongkol, H.R. Li, J.P. Zhang, W.G. Cao, J. Phys. Chem. C 117 (2013) 10502–10511.
[34] B. Li, Z.Y. Ren, Z.X. Ma, X.D. Huang, F. Liu, X.B. Zhang, H.S. Yang, Catal. Sci. Technol. 6 (2016) 1719–1725.
[35] X.J. She, H. Xu, H.F. Wang, J.X. Xia, Y.H. Song, J. Yan, Y.G. Xu, Q. Zhang, D.L. Du, H.M. Li, Dalton Trans. 44 (2015) 7021–7031.
[36] W. She, T.Q.J. Qi, M.X. Cui, P.F. Yan, S.W. Ng, W.Z. Li, G.M. Li, ACS Appl. Mater. Interfaces 10 (2018) 14698–14707.
[37] Y. Geng, X.L. Chen, S.J. Yang, F.D. Liu, W.P. Shan, ACS Appl. Mater. Interfaces 9 (2017) 16952–16959.
[38] C.F. Chen, M.R. Li, Y.S. Jia, R.F. Chong, L.P. Xu, X. Liu, J. Colloid Interface Sci. 564 (2019) 442–453.
[39] K.A.M. Mauke, Y. Lu, K. Kowalski, T. Graule, M. Nachtegaal, O. Kröcher, D. Ferri, ACS Catal. 5 (2015) 5657–5672.
[40] Y.Y. Chai, L. Zhang, Q.Q. Liu, F.L. Yang, W.L. Dai, ACS Sustain. Chem. Eng. 6 (2018) 10526–10535.
[41] H.J. Zhang, L. Liu, Z. Zhou, Phys. Chem. Chem. Phys. 14 (2012) 1286–1292.
[42] S.X. Yu, Y.H. Zhang, F. Dong, M. Li, T.R. Zhang, H.W. Huang, Appl. Catal. B 226 (2018) 441–450.
[43] Z.F. Jiang, C.Z. Zhu, W.M. Wan, K. Qian, J.M. Xie, J. Mater. Chem. A 4 (2016) 1806–1818.
[44] J. Chen, S.H. Shen, P.H. Guo, M. Wang, P. Wu, X.X. Wang, L.J. Guo, Appl. Catal. B 152 (2014) 335–341 153.
[45] J.C. Qian, Z.G. Chen, H. Sun, F. Chen, X. Xu, Z.Y. Wu, P. Li, W.J. Ge, ACS Sustain. Chem. Eng. 6 (2018) 9691–9698.
[46] Y.J. Ma, Y. Bian, Y. Liu, A.Q. Zhu, H. Wu, H. Cui, D.W. Chu, J. Pan, ACS Sustain. Chem. Eng. 6 (2018) 2552–2562.
[47] X.C. Liu, L.X. He, X.M. Chen, L.Q. Du, X.X. Gu, S. Wang, M. Fu, F. Dong, H.Y. Huang, Int. J. Hydrogen Energy 44 (2019) 16154–16163.
[48] J. Luo, X.S. Zhou, L. Ma, X.Y. Xu, RSC Adv. 5 (2015) 68728–68735.
[49] Z. Dai, F. Qin, H.P. Zhao, J. Ding, Y.L. Liu, R. Chen, ACS Catal. 6 (2016) 3180–3192.
[50] M. Sahoo, S. Mansingh, S. Subudhi, P. Mohapatra, K. Parida, Catal. Sci. Technol. 9 (2019) 4678–4692.
[51] G.W. An, M.A. Mahadika, G.X. Piao, W.S. Chae, H. Park, M. Cho, H.S. Chung, J.S. Jan, Appl. Surf. Sci. 480 (2019) 1–12.
[52] Y.C. Chen, Y.C. Pu, Y.J. Hsu, J. Phys. Chem. C 116 (2012) 2967–2975.
[53] J.J. Zhang, T.Q. Zhao, L.C. Zou, S.C. Gan, J. Photochem. Photobiol. A 314 (2016) 35–41.
[54] G. Liu, P. Niu, C.H. Sun, S.C. Smith, Z.G. Chen, G.Q. Lu, H.M. Cheng, J. Am. Chem. Soc. 132 (2010) 11642–11648.
[55] L. Wang, J. Ding, Y.Y. Chai, Q.Q. Liu, J. Ren, X. Liu, W.L. Dai, Dalton Trans. 44 (2015) 11223–11234.
[56] S.C. Hu, F. Zhou, L.Z. Wang, J.L. Zhang, Catal. Commun. 12 (2011) 794–797.
[57] X. Liu, A.L. Jin, Y.S. Jia, T.L. Xia, C.X. Deng, M.H. Zhu, C.F. Chen, X.S. Chen, Appl. Surf. Sci. 405 (2017) 359–371.
[58] A.P. Singh, N. Kodan, B.R. Mehta, A. Held, L. Mayrhofer, M. Moseler, ACS Catal. 6 (2016) 5311–5318.
[59] T.V.M. Sreekanth, P.C. Nagajyothi, G.R. Dillip, Y.R. Lee, J. Phys. Chem. C 121 (2017) 25229–25242.
[60] Y.Z. Zhang, J.N. Gao, Z.W. Chen, J. Colloid Interface Sci. 535 (2019) 331–340.
[61] I. Khan, N. Baig, A. Qurashi, ACS Appl. Energy Mater. 2 (2018) 607–615.